Title

Foreground-Immune Cosmic Microwave Background Lensing with Shear-Only Reconstruction

Journal

Physical Review Letters, 122(18)

ISSN

0031-9007

Authors

Schaan, Emmanuel

Ferraro, Simone

Publication Date

2019-05-10

DOI

10.1103/physrevlett.122.181301

Peer reviewed

Foreground-immune CMB lensing with shear-only reconstruction

Emmanuel Schaan[1, 2, *] and Simone Ferraro[3, 2, †]

[1] *Lawrence Berkeley National Laboratory, One Cyclotron Road, Berkeley, CA 94720, USA*
[2] *Berkeley Center for Cosmological Physics, University of California, Berkeley, CA 94720, USA*
[3] *Department of Astronomy and Miller Institute, University of California, Berkeley, CA 94720, USA*

CMB lensing from current and upcoming wide-field CMB experiments such as AdvACT, SPT-3G and Simons Observatory relies primarily on temperature, rather than polarization. In this regime, foreground contamination to the temperature maps produces significant lensing biases, which cannot be fully controlled by multi-frequency component separation, masking or bias hardening.

In this letter, we use the different symmetries of the lensed CMB and foregrounds to argue that a shear-only estimator should be approximately immune to foregrounds. Using simulations, we build a new method to compute separately and without noise the primary, secondary and trispectrum biases to CMB lensing. We show that the shear estimator is indeed insensitive to foregrounds, even when applied to a single-frequency temperature map contaminated with CIB, tSZ, kSZ and radio point sources. This dramatic reduction in foreground biases allows us to include higher temperature multipoles than with the standard quadratic estimator, thus increasing the overall statistical power of lensing measurements. In addition, the corresponding magnification-only estimator is highly sensitive to foregrounds, and therefore provides a useful diagnostic for potential residuals.

I. INTRODUCTION

Weak lensing of the CMB measures the projected matter distribution throughout the observable Universe, and is one of the most promising probes of dark energy, modified gravity and neutrino masses [1, 2]. As the measurement precision increases, systematic biases become more important. While CMB S4 [3] lensing data should be polarization-dominated in the future, in the coming decade, CMB lensing measurements from AdvACT [4], SPT-3G [5] and Simons Observatory [1] will rely predominantly on temperature. In this regime, foregrounds such as the cosmic infrared background (CIB), the thermal Sunyaev-Zel'dovich effect (tSZ), the kinematic Sunyaev-Zel'dovich effect (kSZ) and radio point sources (PS) can produce biases much larger than the statistical errors, if unaccounted for [6–9]. Mitigation methods such as multi-frequency component separation [9], masking, and bias hardening [7, 11] are sufficient to null the tSZ and radio PS biases, but only partially cancel the CIB, and have no effect on the kSZ, which alone causes a significant bias [8]. New methods are therefore needed, in order to produce unbiased CMB lensing measurements.

In this letter, we explore a different approach, by leveraging the symmetries of the lensing deflections. While the standard quadratic estimator for lensing (QE, [12]) optimally combines information from the shearing and magnification of hot and cold spots of the CMB, we instead estimate shear and magnification separately, as shown in [13–15]. Related work on lensing reconstruction from shear estimators include [13, 19–21]. Intuitively, foregrounds with isotropic 2D power spectra should only bias the magnification estimator, leaving the shear estimator unaffected. The shear estimator should thus provide a robust probe of lensing, and the magnification estimator a sensitive diagnostic for residual foregrounds.

To test this hypothesis, we use simulated maps of the CIB, tSZ, kSZ, radio PS and CMB lensing convergence, including realistic non-Gaussianities and correlations among them, from [22].

II. CMB SHEAR & MAGNIFICATION

In this section, we review the shear and magnification estimators of [14, 15], compare their signal-to-noise and explain heuristically why the shear estimator is expected to be insensitive to foregrounds.

Estimators

Consider the 'large-scale lens regime', where the convergence field is roughly uniform over a patch of the sky containing many CMB hot and cold spots. This is the regime $L \ll \ell$, where L and ℓ are the convergence and temperature map multipoles, respectively. In this limit, lensing produces the following off-diagonal correlations in the lensed temperature T [14, 15]:

$$\begin{aligned}
&\langle T_{\boldsymbol{\ell}+\frac{\boldsymbol{L}}{2}} T_{\frac{\boldsymbol{L}}{2}-\boldsymbol{\ell}}\rangle \\
&= \kappa_{\boldsymbol{L}} \left(\frac{-2\boldsymbol{L}}{L^2}\right) \cdot \left[\left(\boldsymbol{\ell}+\frac{\boldsymbol{L}}{2}\right) C^0_{|\boldsymbol{\ell}+\frac{\boldsymbol{L}}{2}|} + \left(\frac{\boldsymbol{L}}{2}-\boldsymbol{\ell}\right) C^0_{|\frac{\boldsymbol{L}}{2}-\boldsymbol{\ell}|}\right] + \mathcal{O}(\kappa^2) \\
&= C^0_\ell \left[\underbrace{\kappa_{\boldsymbol{L}} \frac{\partial \ln \ell^2 C^0_\ell}{\partial \ln \ell}}_{\substack{\text{isotropic}\\ \text{magnification}}} + \underbrace{\kappa_{\boldsymbol{L}} \cos 2\theta_{\boldsymbol{L},\boldsymbol{\ell}} \frac{\partial \ln C^0_\ell}{\partial \ln \ell}}_{\substack{\text{anisotropic}\\ \text{shear}}}\right] + \mathcal{O}\left(\kappa^2, \left(\frac{L}{\ell}\right)^2\right),
\end{aligned} \tag{1}$$

* eschaan@lbl.gov
† sferraro@berkeley.edu

[1] https://simonsobservatory.org/index.html

where C^0 is the unlensed power spectrum, $\kappa_{\boldsymbol{L}}$ the lensing convergence, and $\theta_{\boldsymbol{L},\boldsymbol{\ell}}$ the angle between vectors $\boldsymbol{L}$ and $\boldsymbol{\ell}$. The first line is exact, to first order in κ. The second line is approximate, valid only in the large-scale lens regime $L \ll \ell$, but highlights the distinct effects of isotropic magnification [2] (independent of $\theta_{\boldsymbol{L},\boldsymbol{\ell}}$) and anisotropic shear ($\propto \cos 2\theta_{\boldsymbol{L},\boldsymbol{\ell}}$), as in galaxy lensing. Because lensing is characterized by only one scalar field (e.g., $\kappa_{\boldsymbol{L}}$), shear and magnification are related, and the QE measures both effects simultaneously. However, foreground contamination will affect magnification and shear differently, so we estimate them separately. Quadratic estimators sensitive only to shear or magnification can be built as:

$$\kappa_{\boldsymbol{L}}^{\text{shear/magnification}} = \left(\frac{L^2}{2}\right) \frac{\int \frac{d^2\boldsymbol{\ell}}{(2\pi)^2}\, T_{\boldsymbol{\ell}} T_{\boldsymbol{L}-\boldsymbol{\ell}}\, g_{\boldsymbol{\ell}}}{\boldsymbol{L}\cdot \int \frac{d^2\boldsymbol{\ell}}{(2\pi)^2}\, (\boldsymbol{L}-\boldsymbol{\ell})\, C^0_{\boldsymbol{L}-\boldsymbol{\ell}}\, g_{\boldsymbol{\ell}}}, \tag{2}$$

where

$$\begin{cases} g_{\boldsymbol{\ell}}^{\text{magnification}} = \dfrac{C_\ell^0}{2(C_\ell^{\text{total}})^2} \dfrac{\partial \ln \ell^2 C_\ell^0}{\partial \ln \ell}, \\ g_{\boldsymbol{\ell}}^{\text{shear}} = \cos(2\theta_{\boldsymbol{L},\boldsymbol{\ell}}) \dfrac{C_\ell^0}{2(C_\ell^{\text{total}})^2} \dfrac{\partial \ln C_\ell^0}{\partial \ln \ell}. \end{cases} \tag{3}$$

These match the harmonic-space version of [14, 15], after normalizing them to be unbiased and substituting $T_{\boldsymbol{\ell}} T_{\boldsymbol{L}-\boldsymbol{\ell}}$ to $T_{\boldsymbol{\ell}+\boldsymbol{L}/2} T_{\boldsymbol{L}/2-\boldsymbol{\ell}}$, to permit fast evaluation as convolutions with FFT. We further substitute the lensed CMB power spectrum to C^0, as is customary for the QE [16, 17]. The magnification estimator effectively measures monopolar distortions of the small-scale CMB power spectrum, while the shear estimator measures quadrupolar distortions, thanks to the $\cos(2\theta_{\boldsymbol{L},\boldsymbol{\ell}})$ weighting. While the estimators in Eq. 2 are only interpreted as shear/magnification estimators in the large-scale limit, they are still unbiased estimators of $\kappa_{\boldsymbol{L}}$ on all scales.

Throughout this letter, we consider an upcoming stage 3 ('CMB S3') experiment, with $1.4'$ beam FWHM and $7\mu K'$ sensitivity at 148GHz. We apply the lensing estimators to the single-frequency map at 148GHz, without any multi-frequency component separation. For the lensing weights, we include the lensed CMB, all the foregrounds of Sec. III and the detector white noise in the total power spectrum.

[2] To be consistent with the optical lensing literature, this effect should really be called 'convergence' instead of 'magnification'. Since we already use the namagnificationme 'convergence' to designate the lensing field κ that is being reconstructed, we decided to call shear and magnification the two distinct effects, to avoid confusion.

Statistical signal-to-noise

As can be seen in Eq. (1), a scale-invariant power spectrum ($\partial \ln \ell^2 C_\ell^0 / \partial \ln \ell = 0$) is not affected by magnification, while a white spectrum ($\partial \ln C_\ell^0 / \partial \ln \ell = 0$) is not affected by shear. The unlensed CMB power spectrum is neither white nor scale-invariant, so a similar signal-to-noise is expected for the shear and magnification estimators. Indeed, as shown in Fig. 1, the lensing noise in shear and magnification is comparable. This is convenient: the shear and magnification can be compared as a consistency check for residual foregrounds. At fixed $\ell_{\text{max},T}$, the total signal-to-noise in shear and magnification is similar, and about 60% of that in the QE, including the cosmic variance. However, as we show below, the shear estimator is less affected by foregrounds, allowing to use $\ell_{\text{max},T} = 3500$ instead of $\ell_{\text{max},T} = 2500$ for the QE. Overall, the signal-to-noise in shear with $\ell_{\text{max},T} = 3500$ is larger than that in QE with $\ell_{\text{max},T} = 2500$ by 10%. To optimize further, one may combine the QE with $\ell_{\text{max},T} = 2000$ to the shear measured from $\ell = 2000 - 3500$. This 'hybrid' estimator, shown in Fig. 1, increases the SNR by 37% compared to the QE with $\ell_{\text{max},T} = 2500$, from 70 to 96, equivalent to almost doubling the survey area.

Expected sensitivity to foregrounds

Because a power spectrum is necessarily positive, any residual foreground causes an excess power spectrum monopole in the CMB map. From Eq. (1), since the CMB is very steep ($\partial \ln \ell^2 C_\ell^0 / \partial \ln \ell < 0$) over the scales of interest ($\ell \gtrsim 1000$), this excess monopole power is then mistaken for a negative magnification, thus producing a negative bias in the QE and magnification estimators.

On the other hand, foregrounds with isotropic 2D power spectra produce no quadrupole power, and therefore do not bias the shear estimator. This is the case if the foreground sources have azimuthally-symmetric emission profiles, and are unclustered (Poissonian) or isotropically clustered. If the foreground sources have independent random ellipticities, they will produce extra noise in the shear estimator, analogous to the shape noise in galaxy lensing (but no bias). The same occurs for example if the foreground objects are point-like but clustered in elliptical filaments with random orientations. On the other hand, any quadrupolar halo profile or halo clustering, aligned with the local tidal field, would bias the shear estimator, analogously to intrinsic alignments in galaxy lensing (see App. D in [26]).

In summary, any residual foreground causes a negative bias in the QE and magnification estimators, whereas only foregrounds with very specific anisotropies can affect the shear estimator. We quantify this intuition in the next section.

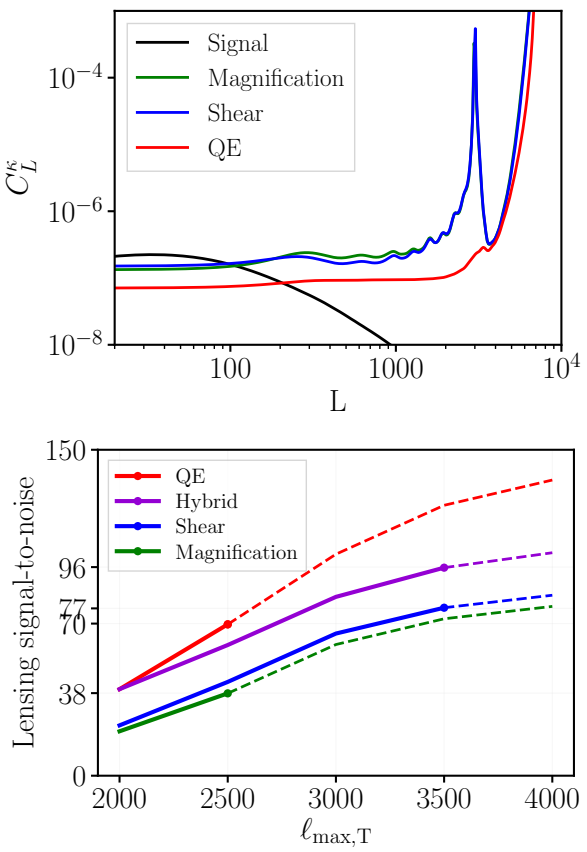

FIG. 1. **Top:** Lensing reconstruction noise per lensing multipole for the standard quadratic estimator (QE, red), the shear (blue) and magnification (green) estimators, when using temperature modes $\ell = 30 - 3500$.
Bottom: Total signal-to-noise on the amplitude of the lensing power spectrum, including cosmic variance, as a function of the maximum temperature multipole $\ell_{\rm max,T}$. Different colors correspond to the different estimators. Dashed lines indicate when foreground biases are larger than the statistical uncertainty. At fixed $\ell_{\rm max,T}$, the signal-to-noise in shear and magnification is similar, and is about 60% of the signal-to-noise of the QE. However, as we show below, keeping the foreground bias below the statistical error requires $\ell_{\rm max,T} = 2500$ for the QE (red dot, $S/N = 70$), compared to $\ell_{\rm max,T} = 3500$ for the shear estimator (blue dot, $S/N = 77$): hence the final shear signal-to-noise exceeds that of the QE by 10%. A hybrid estimator QE($\ell \leq 2000$) & shear($\ell = 2000 - 3500$) is shown in purple, and increases the signal-to-noise by 37% compared to the standard QE($\ell \leq 2500$).
For both panels, we assumed an upcoming CMB S3 experiment with $1.4'$ beam FWHM and 7 $\mu K'$ white noise.

III. SENSITIVITY TO FOREGROUNDS: SIMULATIONS

Method

We use simulated maps of lensing convergence, CIB, tSZ, kSZ and radio PS at 148GHz from [22], obtained by painting spherically-symmetric baryonic profiles on a large-box ($L = 1$ Gpc$/h$) N-body simulation. A halo catalog from this N-body simulation is also available. We re-weight these halos to match the redshift distribution of the LSST gold sample, with i-band magnitude $i < 25.3$ [23] ($dn/dz \propto (z/z_0)^2 e^{-z/z_0}/(2z_0)$ with $z_0 = 0.24$), and obtain a projected 'galaxy' number density map δ_g. The 'galaxy bias' measured from this map roughly matches the expected value $b(z) = 1 + 0.84z$ [23]. These maps have two crucial features: they are realistically correlated with each other, and have a reasonable level of non-Gaussianity. The simulations also include the effect of anisotropic clustering of halos inside filaments, but not the possible intrinsic alignments of halo profiles. We expect the latter effect to be a small correction. Our goal is to compute the foreground biases to the cross-correlation of CMB lensing with galaxies $C_L^{\kappa\delta_g}$ and to the CMB lensing auto-spectrum $C_L^{\kappa\kappa}$.

We subtract the mean emission in each foreground map, then rescale the maps by factors ~ 1 to match the power spectrum model of [24] (0.38 for CIB, 0.7 for tSZ, 0.82 for kSZ, 1.1 for radio PS). Following [6], we then mask the point sources with flux $\gtrsim$ 5mJy in each foreground map. The resulting foreground power spectra are shown in Fig. 2. In principle, one should add all the

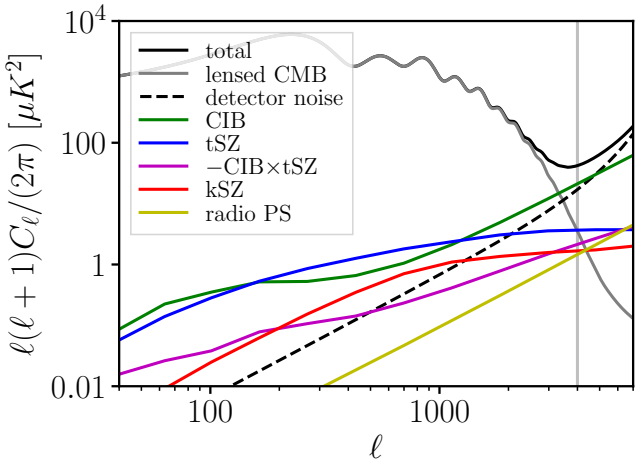

FIG. 2. Power spectrum of the lensed CMB, foregrounds and white detector noise, for an upcoming CMB S3 experiment at 148GHz ($1.4'$ beam FWHM, 7 $\mu K'$ white noise). In each foreground map, point sources with flux greater than 5 mJy have been masked.

foreground maps together to get the total bias, including their correct cross-correlations. However, component separation will reduce each foreground differently. For this reason, we analyze each foreground map separately. This should allow the reader to quantify the foreground bias for any component separation method by rescaling our values appropriately. In what follows, our lens reconstruction relies on temperature multipoles $\ell = 30 - 3500$. To measure the lensing bias due to the foregrounds, we decompose the observed sky temperature $T_{\rm obs}$ into the

lensed primary CMB $T_{\rm CMB}$, the foregrounds T_f and the detector noise $T_{\rm noise}$: $T_{\rm obs} = T_{\rm CMB}+T_f+T_{\rm noise}$. We write $Q[T_A, T_B]$ for any quadratic estimator (QE, shear or magnification) applied to maps T_A and T_B, symmetrized in $A \leftrightarrow B$.

As shown in [6–8], biases to the CMB lensing auto power spectrum $C_L^{\kappa\kappa}$ arise from the foreground *bispectrum* ('primary' and 'secondary' terms), and from the foreground *trispectrum*. We evaluate them as follows:

1) The *primary bispectrum* term is computed as $2\langle Q[T_f, T_f]\ \kappa_{\rm CMB}\rangle$, as in [6–8].

2) The *secondary bispectrum* could in principle be computed as $4\langle Q[T_f, T_{\rm CMB}]\ Q[T_f, T_{\rm CMB}]\rangle$. However, this auto-correlation is biased by the large noise of $Q[T_f, T_{\rm CMB}]$, which would have to be subtracted. We therefore propose and implement a new method to avoid these issues. We Taylor-expand the lensed CMB map $T_{\rm CMB} = T^0 + T^1 + ...$ in powers of κ, and compute the quantity $8\langle Q[T_f, T^0]\ Q[T_f, T^1]\rangle$. This is equivalent, because the quadratic estimators are by construction unbiased when applied to the pair (T^0, T^1). However, the noise is greatly reduced, and this is a cross-correlation so no noise subtraction is needed (no N^0, or higher order bias N^i). We reduce the noise even further by not generating a true Gaussian realization for T^0, but instead fixing the modulus of all the Fourier modes to the square root of the power spectrum.

3) For the *trispectrum* term, we compute $\langle Q[T_f, T_f]\ \ Q[T_f, T_f]\rangle$, and subtract the Gaussian contribution (which is a part of N^0) analytically, as in [6, 7].

For the cross-correlation with tracers $C_L^{\kappa\delta_g}$, only the primary bispectrum is present, and without the combinatorial factor 2: $\langle Q[T_f, T_f]\ \delta_g\rangle$. The secondary bispectrum and trispectrum terms only act as a source of noise on this cross-correlation, not bias.

Results

The resulting foreground biases for the cross-correlation $C_L^{\kappa\delta_g}$ are shown in Fig. 3. Despite the masking, the CIB, tSZ, kSZ and radio PS lead to very large and statistically significant biases for the QE and the magnification estimators. Again, multi-frequency component separation may be used to null the tSZ bias, or reduce the CIB or radio PS biases. However, reducing all these biases simultaneously typically causes a large noise increase. Furthermore, multi-frequency analyses have no effect on the kSZ bias. These foreground biases are therefore a major concern for the standard QE. On the other hand, no foreground bias is detected in the shear estimator. This is the main result of this letter: even when applied to a single-frequency temperature map, the shear estimator measures only the quadrupolar distortions from lensing, and is therefore immune to foregrounds. It is remarkable that this holds even for a single frequency map out to $\ell_{{\rm max},T} = 3500$, where the temperature modes are foreground dominated. Our QE tSZ bias in Fig. 3 is smaller than in [9, 10], which can be explained by our scaling down of the tSZ map to match the power spectrum model of [24], our masking, and the different redshift of our galaxy catalog. Our CIB bias is slightly larger than found in [10].

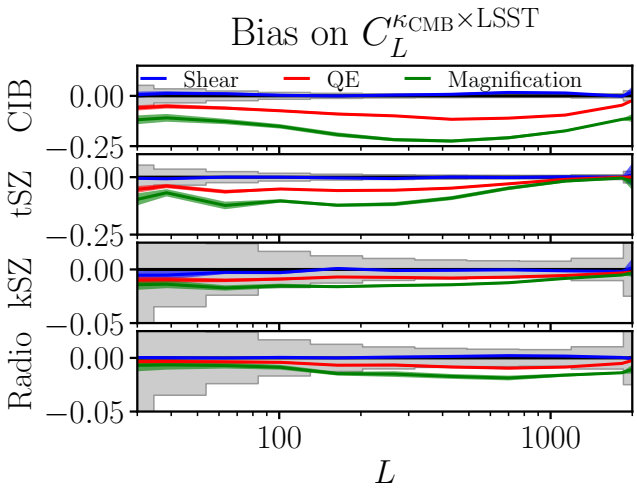

FIG. 3. Relative bias to the cross-correlation between CMB lensing and the LSST gold galaxy sample, as a function of lensing multipole L, when including temperature multipoles $\ell = 30 - 3500$ at 148GHz. This bias corresponds to the 'primary bispectrum' term. The grey boxes indicate bins of lensing multipoles with the corresponding statistical error bars for the standard quadratic estimator (lensing noise plus cosmic variance, identical in each panel). The foreground biases are much larger than the statistical error bars for both the standard quadratic estimator and the magnification estimator, whereas it is barely measurable for the shear estimator.

For the lensing auto-spectrum $C_L^{\kappa\kappa}$, the primary, secondary and trispectrum biases discussed in the previous section are shown in Fig. 4. At low (high) lensing multipoles, the primary (trispectrum) bias dominates. In both cases, a large bias is seen in the QE and magnification estimator, while the shear estimator is unbiased. Our primary and trispectrum foreground biases are consistent with the results of [6] for the CIB and tSZ, and slightly smaller than what found in [8] for the kSZ, due to our rescaling of the kSZ map and the slightly different lensing weights. We compute individually the secondary foreground bias. This term is smaller than the primary and trispectrum term, but non-negligible for L of a few hundred. Here, the shear estimator does not improve over the QE and magnification estimators. Overall, the shear estimator dramatically reduces the foreground biases. As a result, in the absence of any foreground cleaning, the shear estimator allows to increase the range of multipoles used in the lens reconstruction from $\ell_{{\rm max},T} \approx 2500$ for the QE, to $\ell_{{\rm max},T} \approx 3500$ for shear-only. Multi-frequency foreground cleaning can help increase the range of usable multipoles – and thus the statistical power – for both estimators.

IV. CONCLUSION

For current and upcoming CMB experiments such as AdvACT, SPT-3G and Simons Observatory, CMB lensing reconstruction will rely primarily on temperature, rather than polarization. Foreground emission is known to contaminate temperature maps from which lensing is reconstructed, and therefore produce very significant biases, leading to wrong conclusions about cosmology if unaccounted for. Modeling and subtracting these bias terms is likely to be very challenging, due to the complex baryon physics involved in producing them. While some foregrounds can be nulled (tSZ) or reduced (CIB, radio PS) by a multi-frequency analysis, at the cost of a degradation in map noise, other foregrounds cannot (kSZ).

In this letter, we therefore explored a different approach, by using the approximate isotropy of the foreground 2d power spectra, and splitting the QE into isotropic magnification and anisotropic shear estimators [13–15], with similar signal-to-noise ratios. The shear estimator enables a remarkable reduction of foreground biases, compared to the QE, even when applied to a single-frequency temperature map. As a result, the shear estimator allows to increase the range of multipoles used in the lens reconstruction to $\ell_{\mathrm{max},T} \approx 3500$, instead of $\ell_{\mathrm{max},T} \approx 2500$ for the QE, while keeping foreground biases within the statistical uncertainty. Overall, the signal-to-noise in shear with $\ell_{\mathrm{max},T} = 3500$ is larger than that in QE with $\ell_{\mathrm{max},T} = 2500$ by 10%. Component separation may allow the use of higher multipoles for all estimators. The shear estimator thus provides a robust way of measuring lensing. On the other hand, the magnification estimator is highly sensitive to foregrounds, so comparing magnification and shear provides an excellent diagnostic for foreground contamination.

Further optimization is possible, by combining different estimators with different $\ell_{\mathrm{max},T}$. For instance, a hybrid estimator QE($\ell \leq 2000$) & shear($\ell = 2000 - 3500$) improves the lensing signal-to-noise by 37% compared to the standard QE($\ell \leq 2500$), equivalent to almost doubling the survey area. Future CMB lensing data from CMB S4 should be polarization-dominated. The shear and magnification estimators can be generalized to polarization [15], and may bring improvements there too. This would have implications for precision delensing, in order to isolate primordial tensor modes. Finally, similar foreground biases occur in lens reconstruction from intensity mapping [25, 26] (e.g., the 'self-lensing bias' for CIB), and the shear estimator may allow to reduce them [25, 26]. We leave a full exploration of these promising avenues to future work.

ACKNOWLEDGMENTS

We thank Marcelo Alvarez, Simon Foreman, Shirley Ho, Akito Kusaka, Heather Prince, Uroš Seljak, David Spergel, Blake Sherwin, Alex van Engelen, Martin White and Hong-Ming Zhu for useful discussion. ES is supported by the Chamberlain fellowship at Lawrence Berkeley National Laboratory. SF thanks the Miller Institute for Basic Research in Science at the University of California, Berkeley for support.

[1] Lewis, A., & Challinor, A. 2006, Phys. Rep., 429, 1
[2] Hanson, D., Challinor, A., & Lewis, A. 2010, General Relativity and Gravitation, 42, 2197
[3] Abazajian, K. N., Adshead, P., Ahmed, Z., et al. 2016, arXiv:1610.02743
[4] Henderson, S. W., Allison, R., Austermann, J., et al. 2016, Journal of Low Temperature Physics, 184, 772
[5] Benson, B. A., Ade, P. A. R., Ahmed, Z., et al. 2014, Proc. SPIE, 9153, 91531P
[6] van Engelen, A., Bhattacharya, S., Sehgal, N., et al. 2014, ApJ, 786, 13
[7] Osborne, S. J., Hanson, D., & Doré, O. 2014, J. Cosmology Astropart. Phys., 3, 024
[8] Ferraro, S., & Hill, J. C. 2018, Phys. Rev. D, 97, 023512
[9] Madhavacheril, M. S., & Hill, J. C. 2018, arXiv:1802.08230
[10] Baxter, E. J., Omori, Y., Chang, C., et al. 2018, arXiv:1802.05257
[11] Namikawa, T., Hanson, D., & Takahashi, R. 2013, MNRAS, 431, 609
[12] Hu, W., & Okamoto, T. 2002, ApJ, 574, 566
[13] Lu, T., & Pen, U.-L. 2008, MNRAS, 388, 1819
[14] Bucher, M., Carvalho, C. S., Moodley, K., & Remazeilles, M. 2012, Phys. Rev. D, 85, 043016
[15] Prince, H., Moodley, K., Ridl, J., & Bucher, M. 2017, arXiv:1709.02227
[16] Hanson, D., Challinor, A., Efstathiou, G., & Bielewicz, P. 2011, Phys. Rev. D, 83, 043005
[17] Lewis, A., Challinor, A., & Hanson, D. 2011, J. Cosmology Astropart. Phys., 3, 018
[26] Foreman, S., Meerburg, P. D., van Engelen, A., & Meyers, J. 2018, arXiv:1803.04975
[19] Zaldarriaga, M., & Seljak, U. 1999, Phys. Rev. D, 59, 123507
[20] Pen, U.-L. 2004, New A, 9, 417
[21] Lu, T., Pen, U.-L., & Doré, O. 2010, Phys. Rev. D, 81, 123015
[22] Sehgal, N., Bode, P., Das, S., et al. 2010, ApJ, 709, 920
[23] LSST Science Collaboration, Abell, P. A., Allison, J., et al. 2009, arXiv:0912.0201
[24] Dunkley, J., Calabrese, E., Sievers, J., et al. 2013, J. Cosmology Astropart. Phys., 7, 025
[25] Schaan, E., Ferraro, S., & Spergel, D. N. 2018, arXiv:1802.05706
[26] Foreman, S., Meerburg, P. D., van Engelen, A., & Meyers, J. 2018, arXiv:1803.04975

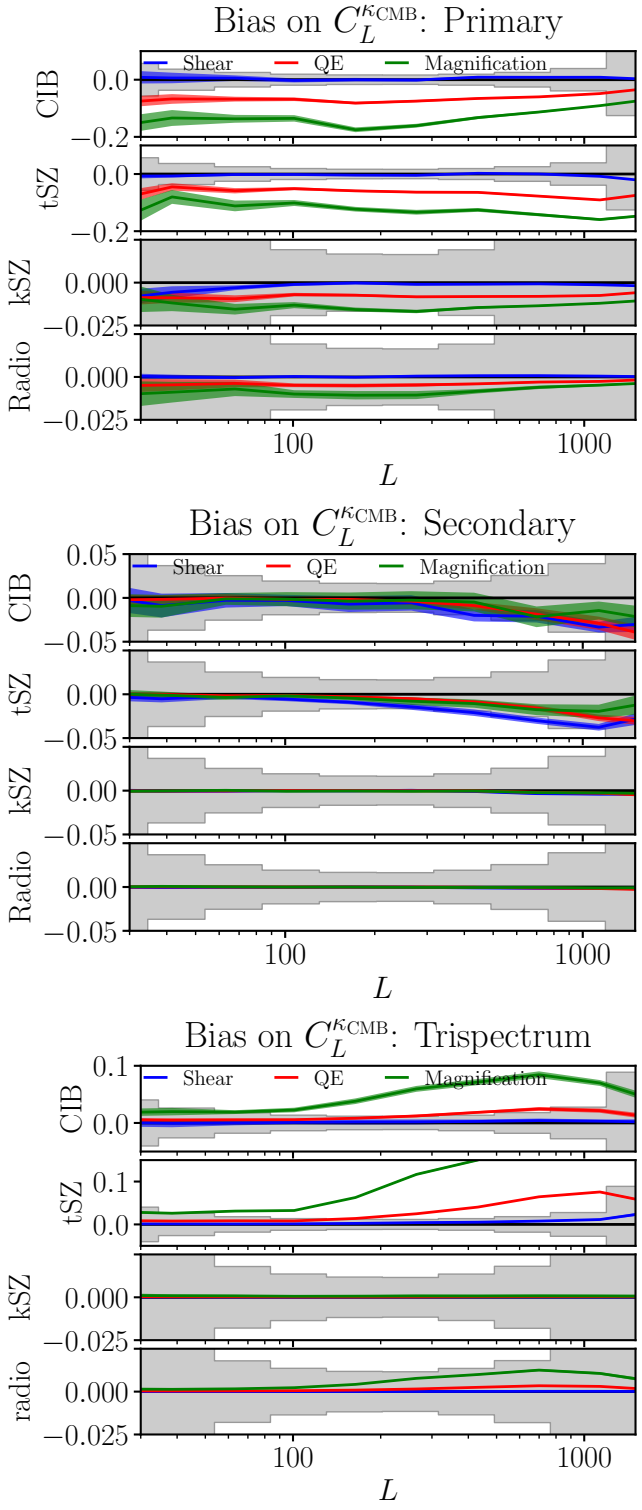

FIG. 4. Relative bias on the CMB lensing power spectrum, as a function of lensing multipole L, when including temperature multipoles $\ell = 30 - 3500$ at 148GHz. The grey boxes indicate bins of lensing multipoles with the corresponding statistical error bars for the standard quadratic estimator (lensing noise plus cosmic variance).
Top: primary bispectrum bias, dominant at low L.
Middle: secondary bispectrum bias.
Bottom: trispectrum bias, dominant at high L.
The dominant biases (primary and trispectrum) are much larger than the statistical error bars for the QE and magnification estimator, and are barely measurable for the shear estimator. The secondary bispectrum bias is smaller, and similar in size for all estimators.

SUPPLEMENTAL MATERIAL

In this supplementary material, we present fast implementations of the shear/magnification estimators using Fast Fourier Transform (FFT), and derive the noise properties of these estimators. We then compare the power spectra of the simulated foreground maps from [22] to the fitting functions from [24], and show sanity checks for our mock LSST gold sample. Finally, we show the overall foreground biases to CMB lensing, as a function of the maximum temperature multipole $\ell_{\mathrm{max},T}$.

Appendix A: Fast evaluation with FFT

For computational efficiency, it is very useful to rewrite the estimators using FFTs, as we describe in this section.

1. Quadratic Estimator

We recast the standard quadratic estimator (QE) into the following form:

$$\hat{\phi}_{\boldsymbol{L}} = N_{\boldsymbol{L}} \int \frac{d^2\boldsymbol{\ell}}{(2\pi)^2} \underbrace{i\boldsymbol{L}\cdot}_{\text{divergence}} \left[\underbrace{\frac{T_{\boldsymbol{L}-\boldsymbol{\ell}}}{C^{\text{total}}_{\boldsymbol{L}-\boldsymbol{\ell}}}}_{\substack{\text{inverse-var.}\\ \text{weighted map}}} \times \underbrace{\frac{C^0_{\boldsymbol{\ell}}}{C^{\text{total}}_{\boldsymbol{\ell}}}\, i\boldsymbol{\ell}\, T_{\boldsymbol{\ell}}}_{\substack{\text{Wiener-filtered}\\ \text{gradient map}}} \right]. \tag{A1}$$

The QE is thus the divergence of the real-space product of the inverse-variance weighted unlensed map by its Wiener-filtered gradient. This is written explicitly as products and convolutions, which can be evaluated efficiently via FFT.

The corresponding reconstruction noise is:

$$N_{\boldsymbol{L}} = \left[\int \frac{d^2\boldsymbol{\ell}}{(2\pi)^2} \frac{f^2_{\boldsymbol{\ell},\boldsymbol{L}-\boldsymbol{\ell}}}{2C^{\text{total}}_{\boldsymbol{\ell}} C^{\text{total}}_{\boldsymbol{L}-\boldsymbol{\ell}}} \right]^{-1}, \tag{A2}$$

where $f_{\boldsymbol{\ell},\boldsymbol{L}-\boldsymbol{\ell}} = -\Big[\boldsymbol{L}\cdot\boldsymbol{\ell} C^0_{\boldsymbol{\ell}} + (\boldsymbol{\ell} \leftarrow \boldsymbol{L}-\boldsymbol{\ell})\Big]$. In order to write this as a sum of products and convolutions, we expand as follows:

$$\begin{aligned} f^2_{\boldsymbol{\ell},\boldsymbol{L}-\boldsymbol{\ell}} &= \Big[\boldsymbol{L}\cdot\boldsymbol{\ell} C^0_{\boldsymbol{\ell}} + (\boldsymbol{\ell} \leftarrow \boldsymbol{L}-\boldsymbol{\ell})\Big]^2 \\ &= (\boldsymbol{L}\cdot\boldsymbol{\ell})^2 {C^0_{\boldsymbol{\ell}}}^2 + (\boldsymbol{L}\cdot\boldsymbol{\ell})[\boldsymbol{L}\cdot(\boldsymbol{L}-\boldsymbol{\ell})] C^0_{\boldsymbol{\ell}} C^0_{\boldsymbol{L}-\boldsymbol{\ell}} + (\boldsymbol{\ell} \leftarrow \boldsymbol{L}-\boldsymbol{\ell}). \end{aligned} \tag{A3}$$

This allows us to rewrite the integrand as a sum of separable terms in $\boldsymbol{\ell}$ and $\boldsymbol{L}-\boldsymbol{\ell}$:

$$\begin{aligned} (N^0_{\boldsymbol{L}})^{-1} = \begin{bmatrix} L_x^2 \\ L_y^2 \\ L_x L_y \end{bmatrix} \cdot \Bigg\{ & \int \frac{d^2\boldsymbol{\ell}}{(2\pi)^2} \begin{bmatrix} \ell_x^2 \\ \ell_y^2 \\ 2\ell_x\ell_y \end{bmatrix} \frac{{C^0_{\boldsymbol{\ell}}}^2}{C^{\text{total}}_{\boldsymbol{\ell}}} \frac{1}{C^{\text{total}}_{\boldsymbol{L}-\boldsymbol{\ell}}} \\ & + \int \frac{d^2\boldsymbol{\ell}}{(2\pi)^2} \begin{bmatrix} \ell_x\,(L_x-\ell_x) \\ \ell_y\,(L_y-\ell_y) \\ 2\ell_x\,(L_y-\ell_y) \end{bmatrix} \frac{C^0_{\boldsymbol{\ell}}}{C^{\text{total}}_{\boldsymbol{\ell}}} \frac{C^0_{\boldsymbol{L}-\boldsymbol{\ell}}}{C^{\text{total}}_{\boldsymbol{L}-\boldsymbol{\ell}}} \Bigg\}. \end{aligned} \tag{A4}$$

This expression is a sum of products and convolutions, which can now be evaluated efficiently via FFT.

2. Shear and magnification estimators

The notions of shear and magnification are only well-defined in the regime where the convergence field is roughly uniform on a patch of the sky containing many CMB hot and cold spots. This occurs when $L \ll \ell$. In this limit, we can Taylor expand the power spectra in L around ℓ:

$$C^0_{|\boldsymbol{\ell}\pm\boldsymbol{L}/2|} = C^0_\ell \left[1 \pm \frac{1}{2} \left(\frac{\boldsymbol{L}\cdot\boldsymbol{\ell}}{\ell^2} \right) \frac{\partial \ln C^0_\ell}{\partial \ln \ell} + \mathcal{O}\left(\frac{L}{\ell} \right)^2 \right]. \tag{A5}$$

As a result, the off-diagonal correlations of the lensed temperature become:

$$\langle T_{\boldsymbol{\ell}+\boldsymbol{L}/2} T^{\star}_{\boldsymbol{\ell}-\boldsymbol{L}/2}\rangle \simeq C^0_\ell \left[\underbrace{\kappa_{\boldsymbol{L}}}_{\substack{\text{isotropic}\\ \text{magnification}}} \frac{\partial \ln \ell^2 C^0_\ell}{\partial \ln \ell} + \underbrace{\kappa_{\boldsymbol{L}} \cos 2\theta_{\boldsymbol{L},\boldsymbol{\ell}}}_{\substack{\text{anisotropic}\\ \text{shear}}} \frac{\partial \ln C^0_\ell}{\partial \ln \ell} \right]. \tag{A6}$$

We can thus distinguish the effects of isotropic magnification (independent of $\theta_{\boldsymbol{L},\boldsymbol{\ell}}$) and anisotropic shear ($\propto \cos 2\theta_{\boldsymbol{L},\boldsymbol{\ell}}$). Given the dependence on $\theta_{\boldsymbol{L},\boldsymbol{\ell}}$, estimators for magnification and shear can be obtained as follows:

$$\kappa^{\text{magnification}}_{\boldsymbol{L}} \equiv \frac{\int \frac{d^2\boldsymbol{\ell}}{(2\pi)^2}\, T_{\boldsymbol{\ell}+\boldsymbol{L}/2} T^*_{\boldsymbol{\ell}-\boldsymbol{L}/2}\, \frac{C^0_\ell}{2(C^{\text{total}}_\ell)^2} \frac{\partial \ln \ell^2 C^0_\ell}{\partial \ln \ell}}{\int \frac{d^2\boldsymbol{\ell}}{(2\pi)^2}\, \frac{(C^0_\ell)^2}{2(C^{\text{total}}_\ell)^2} \left(\frac{\partial \ln \ell^2 C^0_\ell}{\partial \ln \ell}\right)^2}, \tag{A7}$$

and

$$\kappa^{\text{shear}}_{\boldsymbol{L}} \equiv \frac{\int \frac{d^2\boldsymbol{\ell}}{(2\pi)^2}\, T_{\boldsymbol{\ell}+\boldsymbol{L}/2} T^*_{\boldsymbol{\ell}-\boldsymbol{L}/2}\, \cos(2\theta_{\boldsymbol{L},\boldsymbol{\ell}}) \frac{C^0_\ell}{2(C^{\text{total}}_\ell)^2} \frac{\partial \ln C^0_\ell}{\partial \ln \ell}}{\int \frac{d^2\boldsymbol{\ell}}{(2\pi)^2}\, \cos(2\theta_{\boldsymbol{L},\boldsymbol{\ell}})^2 \frac{(C^0_\ell)^2}{2(C^{\text{total}}_\ell)^2} \left(\frac{\partial \ln C^0_\ell}{\partial \ln \ell}\right)^2}. \tag{A8}$$

These quadratic estimators would be the inverse-variance weighted magnification and shear estimators if the variance of $T_{\boldsymbol{\ell}} T_{\boldsymbol{L}-\boldsymbol{\ell}}$ was exactly $2(C^{\text{total}}_\ell)^2$, which is not quite true. A multiplicative factor that makes the estimators above unbiased on all scales can be derived, and is discussed in Sec. A 4.

3. Fast approximate estimators

To enable the use of FFT in the evaluation of the shear and magnification, we further approximate the above expressions as:

$$\kappa^{\text{magnification}}_{\boldsymbol{L}} \equiv \frac{\int \frac{d^2\boldsymbol{\ell}}{(2\pi)^2}\, T_{\boldsymbol{\ell}} T_{\boldsymbol{L}-\boldsymbol{\ell}}\, \frac{C^0_\ell}{2(C^{\text{total}}_\ell)^2} \frac{\partial \ln \ell^2 C^0_\ell}{\partial \ln \ell}}{\int \frac{d^2\boldsymbol{\ell}}{(2\pi)^2}\, \frac{(C^0_\ell)^2}{2(C^{\text{total}}_\ell)^2} \left(\frac{\partial \ln \ell^2 C^0_\ell}{\partial \ln \ell}\right)^2}, \tag{A9}$$

and

$$\kappa^{\text{shear}}_{\boldsymbol{L}} \equiv \frac{\int \frac{d^2\boldsymbol{\ell}}{(2\pi)^2}\, T_{\boldsymbol{\ell}} T_{\boldsymbol{L}-\boldsymbol{\ell}}\, \cos(2\theta_{\boldsymbol{L},\boldsymbol{\ell}}) \frac{C^0_\ell}{2(C^{\text{total}}_\ell)^2} \frac{\partial \ln C^0_\ell}{\partial \ln \ell}}{\int \frac{d^2\boldsymbol{\ell}}{(2\pi)^2}\, \underbrace{\cos(2\theta_{\boldsymbol{L},\boldsymbol{\ell}})^2}_{\to 1/2} \frac{(C^0_\ell)^2}{2(C^{\text{total}}_\ell)^2} \left(\frac{\partial \ln C^0_\ell}{\partial \ln \ell}\right)^2}. \tag{A10}$$

These integrals are evaluated by FFT, using the following replacement:

$$\cos(2\theta_{\boldsymbol{L},\boldsymbol{\ell}}) = 2\frac{(\boldsymbol{L}\cdot\boldsymbol{\ell})^2}{L^2\ell^2} - 1 = \frac{1}{L^2} \begin{bmatrix} L_x^2 - L_y^2 \\ 4L_xL_y \end{bmatrix} \cdot \begin{bmatrix} \ell_x^2 - \ell_y^2 \\ \ell_x\ell_y \end{bmatrix} \frac{1}{\ell^2}, \tag{A11}$$

These estimators make two approximations, beyond the Taylor expansion to first order in $\kappa_{\boldsymbol{L}}$. The first one is the Taylor expansion of the unlensed power spectrum to first order. The second one is the replacement of slightly different ℓ in the temperature maps/weights.

Outside of the large-scale lensing $L \ll \ell$, the first approximation becomes inaccurate, and the shear and magnification acquire a multiplicative bias, which we compute in the next subsection.

On the other hand, the second approximation doesn't introduce any spurious error, to first order in L/ℓ. Indeed, the extra term averages over angle to zero, when multiplied by 1 or $\cos(2\theta)$, as is done in the shear and magnification estimators:

$$\langle T_{\boldsymbol{\ell}} T_{\boldsymbol{L}-\boldsymbol{\ell}}\rangle \simeq C^0_\ell \left[\underbrace{\kappa_{\boldsymbol{L}}}_{\substack{\text{isotropic}\\ \text{magnification}}} \frac{\partial \ln \ell^2 C^0_\ell}{\partial \ln \ell} + \underbrace{\kappa_{\boldsymbol{L}} \cos 2\theta_{\boldsymbol{L},\boldsymbol{\ell}}}_{\substack{\text{anisotropic}\\ \text{shear}}} \frac{\partial \ln C^0_\ell}{\partial \ln \ell} + \underbrace{\kappa_{\boldsymbol{L}} \cos\theta_{\boldsymbol{L},\boldsymbol{\ell}}}_{\substack{\text{additional term}\\ \text{which averages to zero}}} \frac{2L}{\ell} \frac{\partial \ln C^0_\ell}{\partial \ln \ell} + \mathcal{O}\left(\frac{L}{\ell}\right)^2 \right]. \tag{A12}$$

4. Multiplicative bias

Introducing the following simplifying notations

$$\begin{cases} g_{\boldsymbol{\ell}}^{\rm magnification} = \dfrac{C_\ell^0}{2(C_\ell^{\rm total})^2}\dfrac{\partial \ln \ell^2 C_\ell^0}{\partial \ln \ell}, \\ g_{\boldsymbol{\ell}}^{\rm shear} = \cos(2\theta_{\boldsymbol{L},\boldsymbol{\ell}})\dfrac{C_\ell^0}{2(C_\ell^{\rm total})^2}\dfrac{\partial \ln C_\ell^0}{\partial \ln \ell}, \end{cases} \tag{A13}$$

the quadratic estimators for shear/magnification can be written as:

$$\kappa_{\boldsymbol{L}}^{\rm shear/magnification} = \frac{\int \frac{d^2\boldsymbol{\ell}}{(2\pi)^2}\, T_{\boldsymbol{\ell}} T_{\boldsymbol{L}-\boldsymbol{\ell}}\, g_{\boldsymbol{\ell}}}{\int \frac{d^2\boldsymbol{\ell}}{(2\pi)^2}\, C_\ell^{\rm total} g_{\boldsymbol{\ell}}^2}. \tag{A14}$$

Since $\langle T_{\boldsymbol{\ell}} T_{\boldsymbol{L}-\boldsymbol{\ell}}\rangle = \phi_{\boldsymbol{L}} f_{\boldsymbol{\ell},\boldsymbol{L}-\boldsymbol{\ell}}$, we obtain the multiplicative bias of the estimator:

$$\langle \kappa_{\boldsymbol{L}}\rangle^{\rm shear/magnification} = \kappa_{\boldsymbol{L}}^{\rm true}\left(\frac{-2}{L^2}\right)\frac{\int \frac{d^2\boldsymbol{\ell}}{(2\pi)^2}\, f_{\boldsymbol{\ell},\boldsymbol{L}-\boldsymbol{\ell}}\, g_{\boldsymbol{\ell}}}{\int \frac{d^2\boldsymbol{\ell}}{(2\pi)^2}\, C_\ell^{\rm total} g_{\boldsymbol{\ell}}^2}, \tag{A15}$$

where again $f_{\boldsymbol{\ell},\boldsymbol{L}-\boldsymbol{\ell}} = -\Big[\boldsymbol{L}\cdot\boldsymbol{\ell} C_{\boldsymbol{\ell}}^0 + (\boldsymbol{\ell} \leftarrow \boldsymbol{L}-\boldsymbol{\ell})\Big]$. Finally:

$$\langle \kappa_{\boldsymbol{L}}\rangle^{\rm shear/magnification} = \kappa_{\boldsymbol{L}}^{\rm true}\left(\frac{2}{L^2}\right)\frac{\boldsymbol{L}\cdot\int \frac{d^2\boldsymbol{\ell}}{(2\pi)^2}\, (\boldsymbol{L}-\boldsymbol{\ell})\, C_{\boldsymbol{L}-\boldsymbol{\ell}}^0\, g_{\boldsymbol{\ell}}}{\int \frac{d^2\boldsymbol{\ell}}{(2\pi)^2}\, C_\ell^{\rm total} g_{\boldsymbol{\ell}}^2}. \tag{A16}$$

This can again be evaluated with FFT.

5. Bias-corrected shear and magnification estimators

Correcting the multiplicative bias gives the following estimators for shear and magnification:

$$\kappa_{\boldsymbol{L}}^{\rm shear/magnification} = \left(\frac{L^2}{2}\right)\frac{\int \frac{d^2\boldsymbol{\ell}}{(2\pi)^2}\, T_{\boldsymbol{\ell}} T_{\boldsymbol{L}-\boldsymbol{\ell}}\, g_{\boldsymbol{\ell}}}{\boldsymbol{L}\cdot\int \frac{d^2\boldsymbol{\ell}}{(2\pi)^2}\, (\boldsymbol{L}-\boldsymbol{\ell})\, C_{\boldsymbol{L}-\boldsymbol{\ell}}^0\, g_{\boldsymbol{\ell}}}, \tag{A17}$$

where the $g_{\boldsymbol{\ell}}$ functions are defined above. This is the estimator used in the paper.

6. Noise power spectrum

The shear and magnification estimators, corrected for multiplicative bias or not, are of the form

$$\kappa_{\boldsymbol{L}}^{\rm shear/magnification} = \int \frac{d^2\boldsymbol{\ell}}{(2\pi)^2}\, T_{\boldsymbol{\ell}} T_{\boldsymbol{L}-\boldsymbol{\ell}}\, g_{\boldsymbol{\ell}} \;\; /\text{normalization}. \tag{A18}$$

We thus find the noise power spectrum to be

$$N_L^{\kappa^{\rm shear/magnification}} = \int \frac{d^2\boldsymbol{\ell}}{(2\pi)^2}\, C_{\boldsymbol{\ell}}^{\rm total} C_{\boldsymbol{L}-\boldsymbol{\ell}}^{\rm total}\; g_{\boldsymbol{\ell}}\Big(g_{\boldsymbol{\ell}} + g_{\boldsymbol{L}-\boldsymbol{\ell}}\Big) \;\; /\text{normalization}^2. \tag{A19}$$

In Fig. 5, we show that these analytical expressions for the noise power spectrum match the measured power spectrum of the estimator, when applied to mock Gaussian CMB maps with power spectrum equal to the total power spectrum (lensed CMB + detector noise + foregrounds).

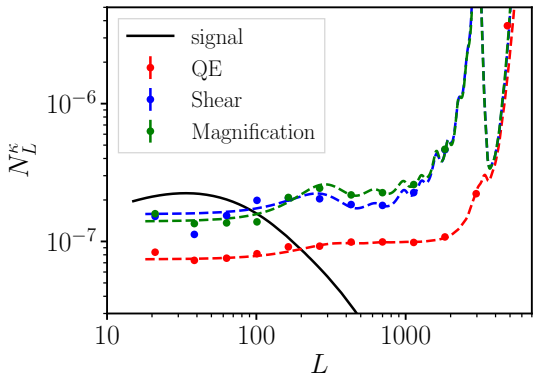

FIG. 5. Comparison of the measured noise power spectrum for the QE, shear and magnification (data points) with the analytical prediction (dashed lines). This validates our pipeline for the QE, shear and magnification estimators, and for the analytical noise calculations.

Appendix B: Foreground spectra

We compute the power spectra of the various foreground maps from [22], before masking, and multiply them by factors of order unity (0.38 for CIB, 0.7 for tSZ, 0.82 for kSZ, 1.1 for radio PS) to match the spectra from [24]. After masking, the resulting power spectra are shown in Fig. 6, and compared to the spectra from [24]. At the power spectrum level, the effect of masking is most spectacular for the radio PS. However, while masking may not change the foreground power much, it may have a larger effect on the foreground bispectrum and trispectrum.

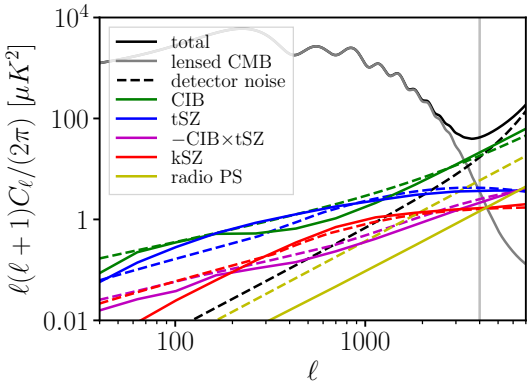

FIG. 6. We fixed the normalization of the Sehgal maps [22] to match the power spectrum model from [24] (dashed lines). The Sehgal maps were subsequently masked for point sources above 5mJy, producing the solid curves shown in this figure. At the power spectrum level, the effect of masking is most visible on the radio PS.

Appendix C: Galaxy catalog

To construct a mock LSST gold sample, we re-weight the halos in the catalog from [22] to match the redshift distribution of the LSST gold sample, with i-band magnitude $i < 25.3$ [23]:

$$\frac{dn}{dz} \propto \frac{1}{2z_0}\left(\frac{z}{z_0}\right)^2 e^{-z/z_0} \text{ , with } z_0 = 0.24. \tag{C1}$$

The expected galaxy bias for the LSST sample is $b(z) = 1 + 0.84z$ [23], and Fig. 7 shows that our reweighted mock catalog has approximately the same bias.

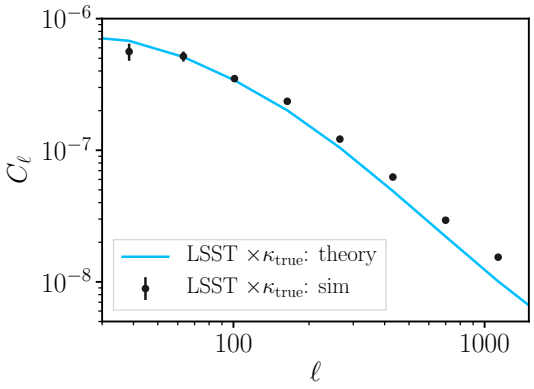

FIG. 7. Cross correlation between our mock LSST gold sample, constructed by reweighting the halos in the catalog from [22], and the CMB lensing convergence in the simulations. The solid line shows the theory expectation for the actual LSST gold sample [23]. The rough agreement implies that the bias of the reweighted sample is close to the one of LSST sources, which is sufficient to estimate the foreground biases to LSST$\times\kappa_{\rm CMB}$.

Appendix D: Foreground biases to the lensing amplitude

We show the bias on the amplitude of the lensing power spectrum and the amplitude of the cross-power spectrum of CMB lensing and LSST gold galaxies in Fig 8. Considering the lensing auto-spectrum, the foreground bias equal the statistical uncertainty (including cosmic variance) for $\ell_{\rm max,}{}_T = 2500$ for the QE and magnification, compared to $\ell_{\rm max,}{}_T = 3500$ for the shear estimator. This increase in $\ell_{\rm max,}{}_T$ has important implications in terms of lensing signal-to-noise, as described in the main text.

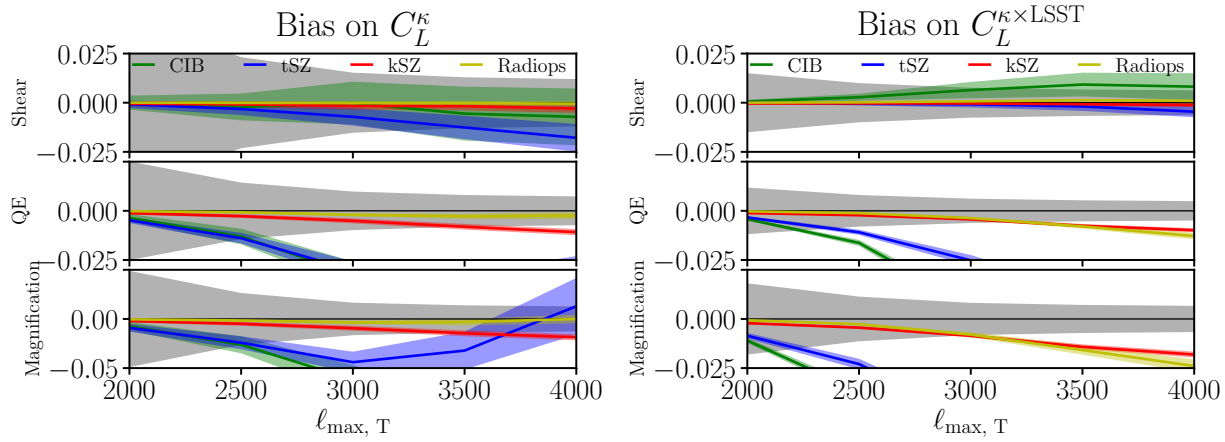

FIG. 8. Relative bias on the amplitude of the lensing power spectrum (left) and the amplitude of the cross-power spectrum of CMB lensing and LSST gold galaxies (right) due to the various foregrounds. The grey band is the statistical error, including cosmic variance.